




INTEGRATION OF SEISMIC DATA TO BUILD GEOMECHANICAL MODELS FOR THE BRAZILIAN PRE-SALT RESERVOIRS – AN EXAMPLE IN THE SANTOS BASIN

Talles Barsanti Meneguim ^{1,2}, Thelson Luiz Pinheiro de Almeida¹,
Renata dos Santos Giacomel¹, Viviane Kotani Shimizu¹, Antonio Mauricio Nabuco Tartarini¹,
Alexandre Rodrigo Maul ¹, and Raquel Quadros Velloso ²

ABSTRACT. Pre-Salt Province hydrocarbon accumulations increased the relevance of E&P activities in the Santos Basin, Brazil. Deep carbonatic reservoirs, below 5 km, located in ultra-deep water of over than 2 km, under a salt section varying from few meters to 3 km of thickness compose this hydrocarbon province. Geomechanical models representing these complexities require a teamwork within an integrated environment of geosciences and engineering. In this context, despite being indirect measurements, high-definition seismic data allows us to add valuable content to build reliable geomechanical models. In the short-term, during drilling and completion phases, it is mandatory to model potential geohazards related with high porosity sands; intercalations of different hardness rock types in shales, sandstone, and marls; and highly creep soluble salts behaviors. These effects are responsible for pipe sticking, project profit losses and seabed facilities risks. Long-term risks are modelled accessing the uncertainty in the static elastic properties from seismic attributes. Here, we choose three different dynamics vs. static equivalences giving more reality to the model, delivering information about seabed subsidence, seal rock failures, post-salt fault/fracture reactivations and well casing damages. In this work, we demonstrate the discipline integration starting from the seismic data to model these geomechanical scenarios.

Keywords: geomechanical modeling, seismic data, geohazards, dynamic vs. static equivalences, Santos Basin pre-salt reservoir.

RESUMO. Acumulações de hidrocarboneto na Província do Pré-Sal aumentaram a relevância da atividade de E&P na Bacia de Santos, Brasil. Reservatórios carbonáticos profundos abaixo de 5 km, coluna d'água ultraprofunda (>2 km), e abaixo da seção salífera com espessura de dezenas de metros até aproximadamente 3 km compõem essa província de hidrocarbonetos. Modelos geomecânicos representando essas complexidades requerem uma equipe multidisciplinar em um ambiente integrando-se geociências e engenharias. Neste contexto, uma medida indireta, dados sísmicos de alta definição agregam conteúdo valioso na modelagem geomecânica. No curto prazo, nas fases de perfuração e completção, é mandatório modelar os potenciais perigos geológicos relacionados com: arenitos de alta porosidade; intercalações de rochas folhelhos, margas e arenitos de diferentes rigidez; e sais solúveis de alta fluência. Essas ocorrências causam prisão da coluna, diminuição dos lucros e danos às instalações no fundo marinho. Riscos de longo prazo são modelados estimando-se a incerteza nas propriedades elásticas estáticas a partir de atributos sísmicos. Escolhemos três diferentes equivalências dinâmica vs. estática, entregando informações mais confiáveis sobre subsidência do leito marinho, integridade da caeadora, reativação de falhas e fraturas e danos a revestimentos de poços. Neste trabalho demonstramos a integração das disciplinas desde o dado sísmico até o modelo geomecânico.

Palavras-chave: modelagem geomecânica, dado sísmico, geohazards, equivalências dinâmica vs. estática, pré-sal da Bacia de Santos.

*Corresponding author: Talles Barsanti Meneguim

¹Petrobras - Reservoir Geophysics, Avenida Henrique Valadares, 7º andar, Rio de Janeiro, RJ, 20031-030 Brazil – E-mails: tallesbarsanti@petrobras.com.br, thelsonalmeida@petrobras.com.br, renata.giacomel@petrobras.com.br, vivianeshimizu@petrobras.com.br, antonio.tartarini@petrobras.com.br, alexandre.maul@petrobras.com.br

²Pontifícia Universidade Católica, Rio de Janeiro - PUC-Rio, Department of Civil and Environmental Engineering, Rua Marquês de São Vicente, 225 – Gávea Rio de Janeiro, RJ, 22451-900 Brazil – E-mail: raquelveloso@puc-rio.br

INTRODUCTION

The proven oil and gas reserves have more than doubled from 2000 to 2014 in Brazil mainly due to carbonatic pre-salt reservoirs (ANP, 2003, 2015). The pre-salt carbonatic reservoir province of Santos Basin, Brazilian offshore, is constituted by deep accumulations situated vertically below 5 km, considering the sea level, and is located in an ultra-deep-water column of more than 2 km (Carminatti et al., 2008). This offshore portion of the Santos Basin has a complex stratigraphic column above the carbonatic pre-salt reservoirs. It is mainly composed by a huge evaporitic section presenting thickness varying from dozens of meters to close to 3 km, with an average thickness around 2.5 km (Mohriak et al., 2012). Besides important carbonatic rafts above this salt section, it presents intercalated siliciclastic deposits above the mentioned raft occurrences (Moreira et al., 2007). The location of the Santos Basin pre-salt reservoir and the study area are illustrated in Figure 1. Figure 2 shows the geological complexity in the studied area to be considered when processing the geomechanical model. The evaporitic section acts as seals for the carbonatic pre-salt reservoirs (Carminatti et al., 2008).

A relevant issue in hydrocarbon field's development and production is how to keep the field oil or gas volume production and the business value in the same time that the security in seabed facilities, pipelines, platforms, and environment is being guaranteed (Zoback, 2007). One of the most known attempts regarding this matter is the maintenance of pore pressure by fluid injection avoiding the decrease of the effective stress, which may result in excessive deformation (compaction), reduction of the permeability and productivity of the reservoir and some important subsurface geologic hazards, which must be addressed in the offshore Santos Basin. The short-term geologic hazards may occur during the well drilling and completion phases. Among these, we can mention shallow-water flow (SWF) from over pressured high permo-porous sandstones, and drift diameter of the inside borehole wall from intercalation of different hardness rock types, like shales, sandstones, and marls. Besides these,

there is also loss of fluid circulation in uncontrolled flow into fractured/high quality permo-porous rocks, such as sandstones and carbonates containing vugs and pipe sticking by soluble salts such as tachyhydrite, with creep behavior in the evaporitic section. These short-term events are potentially responsible for affecting the seabed facility security, pipelines and platforms also influencing the project business value (Teixeira et al., 2017; Toribio et al., 2017; Meneguim, 2019; Meneguim et al., 2019; Meneguim et al., 2021). Other geomechanical risks are associated with long-term reservoir's production, as seabed subsidence, seal rock failure, post-salt fault/fracture reactivation, reservoir's compaction and well casing damages (Costa & Poiate Jr., 2009). In this work, it was addressed the seismic data usage considering the burial depth behavior to model the geohazards into the post-salt and salt sections, ensuring the project business value as it makes the well operations safer. It was demonstrated the connection between soluble salts and compressional impedance (P-impedance) in the salt section, enabling us to model the salt heterogeneities through a seismic inversion methodology (Meneguim et al., 2017; Teixeira et al., 2017). As per our understanding, it is also essential to establish the equivalence between dynamic elastic properties estimated from seismic data and the static elastic properties which delivers reliable inputs for the long-term reservoir management. To access the uncertainties in the static elastic property estimation from the dynamic seismic attributes in the reservoir, it was chosen three different static vs. dynamic equivalences. The 1st and 2nd dynamic equivalences are well-known parameters coming from scientific journals (Lacy, 1996; Pandula & Mockovčiaková, 2002). The 3rd one was obtained from mechanical tests carried out in the Rock Test Lab of PUC (Pontifical Catholic University of Rio de Janeiro, Rio de Janeiro, Gávea, RJ, Brazil, Department of Civil & Environmental Engineering). It was used roman travertine core samples as mechanical analogues of the good quality carbonate reservoirs since both have the same mineral composition: calcite and the available high

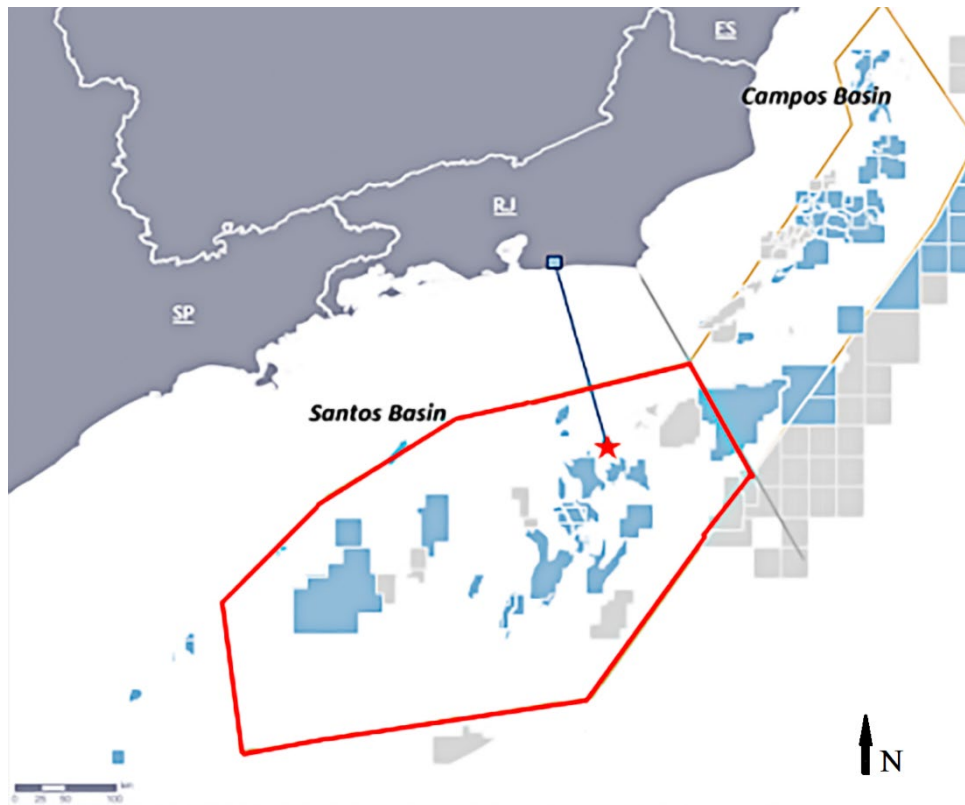


Figure 1 - The pre-salt reservoir province in the Brazilian offshore (grey polygon) and in the Santos Basin (red polygon). The location of the dataset used in this study (red star) is 300 km from Rio de Janeiro city. Most relevant block bids in the Pre-Salt Province are also indicated (blue boxes).

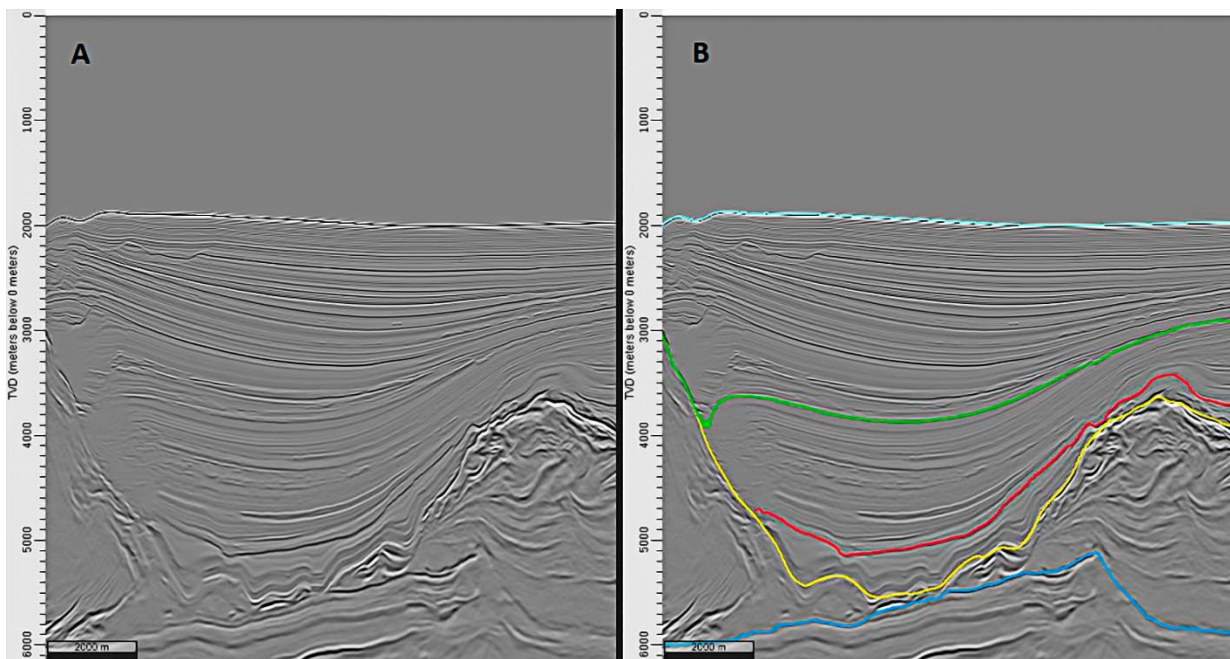


Figure 2 - A – Seismic amplitude section in depth of the study area illustrating the geological complexity. B – Seismic amplitude section in depth presenting interpretations. The light blue horizon reflects the sea level (Marambaia Formation). The light green horizon is the Itajaí-Açu Formation. The red horizon marks the top of the carbonatic rafts of Guarujá Formation. The yellow horizon is the top of the salt section (Ariari Formation), and the dark blue horizon denotes the base of salt, the main reference recognized as the top of the pre-salt reservoir (Barra Velha Formation).

porosity roman travertine with some dissolutions (Meneguim et al., 2019). It was observed a difference around 35% in the elasticity modulus estimation and close to 22% in the Poisson's ratio estimation when comparing the less rigid 3rd equivalence with the most rigid 1st one.

To model all these complexities in 3D, an integrated cooperated teamwork involving many disciplines such as geophysics, geology, reservoir and well engineering is mandatory (Meneguim, 2019; Meneguim et al., 2021).

Therefore, in our analysis it is emphasized the benefits to develop complex geomechanical models and to mitigate reservoir field risks starting from the seismic, geologic, and engineering data.

METHODOLOGY

Figure 3 gives a general scene where our main workflow is located inside the whole geomechanical workflow. In Figure 4, the red box on the left side of Figure 3 is fully detailed since this part of the whole workflow is the main subject in this work.

Figure 4 is the main part of the described workflow, and it is detailed here. Starting with the available angle stack seismic data, P-Velocity, S-Velocity and density well logs as well as the rock types, the wavelets vs. burial depth was established. Then we performed the AVO/AVA seismic inversion, giving us the P and S-impedances and the dynamic elastic parameters: elasticity modulus (E) and Poisson's ratio (ν). The facies model focused on the main geohazards and was built based on seismic attributes from clustering classification or probability density functions using the most likely facies. Finally, the static elastic deformability parameters were obtained from the static vs. dynamic equivalences.

METHODOLOGY APPLICATIONS, RESULTS AND DISCUSSIONS

A relevant issue when integrating seismic data to rock properties is the residual pulse (wavelet) effect, which is responsible for the lateral lobes in seismic amplitude data. Figure 5 shows in "A" the amplitude seismic data in depth using the grayscale

pallet. In "B", it is shown the same section as the previous one but presenting the rough integration of seismic amplitude in rainbow pallet with some expressive lateral lobes pointed out by the white arrows. Finally, in "C" it is shown the acoustic inverted seismic amplitude data. This is within the seismic bandwidth, attempting to remove the lateral lobe effect, as pointed out in the much less expressive events, once again highlighted by the white arrows. Figure 6 shows a magnified view of Figure 5 closer to the seabed illustrating the remotion of the lateral lobe effect. The lateral lobes in wiggle details can also be observed in Figure 7 inside the dashed rectangle illustrating the attenuation of the lateral lobes when seismic inversion is performed.

To estimate the geohazards in the post-salt section, the residual seismic pulse (wavelet) must be removed from the seismic data. Figure 8 illustrates the normalized wavelet frequency spectrum throughout the burial depth (Meneguim et al., 2019). We notice the narrowing of the frequency bandwidth mainly at high frequencies throughout the burial depth.

We will focus our attention on the following geologic hazards in the post-salt section related to short-term events during the drilling and completion phases:

1. **Drift Diameter** - Unappropriated eccentricity of the inside wall of a borehole. Tools, casing, and smaller pipes cannot be passed through the borehole. It has potential for pipe sticking on intercalations of different hardness rock types (shales, sandstones and marls).
2. **Lost Circulation** - Uncontrolled flow of mud into fractured formations and high quality permo-porous rocks such as sandstones and carbonates containing vugs.
3. **Kick** - caused by Shallow-Water Flow (SWF). Uncontrolled water flow from over pressured and high quality permo-porous sandstones into the well.
4. **Pipe Sticking** - by soluble salts (tachyhydrite) with creep behavior in the salt section.

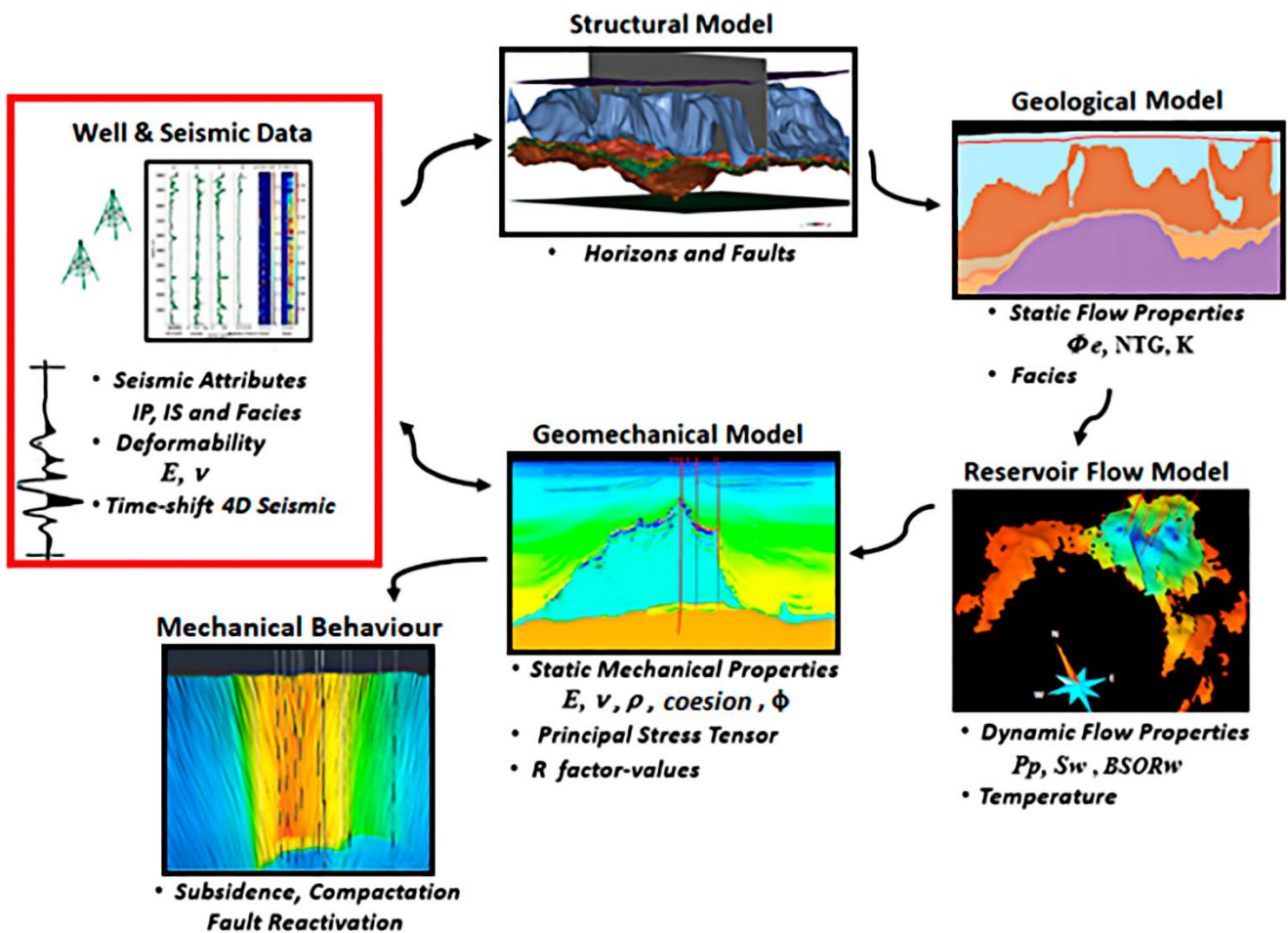


Figure 3 - Overview of the Geomechanical Modeling Workflow. The red box on the left side is the main subject in this work.

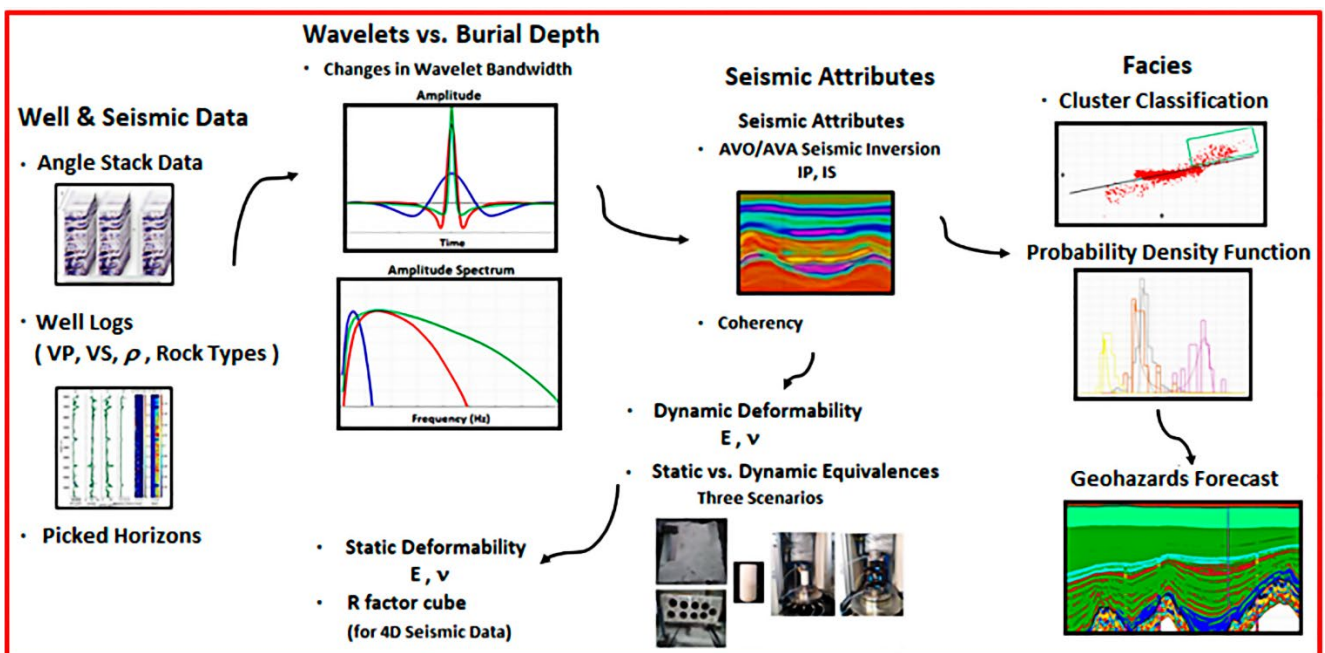


Figure 4 - The workflow developed in this work starting from seismic and well data.

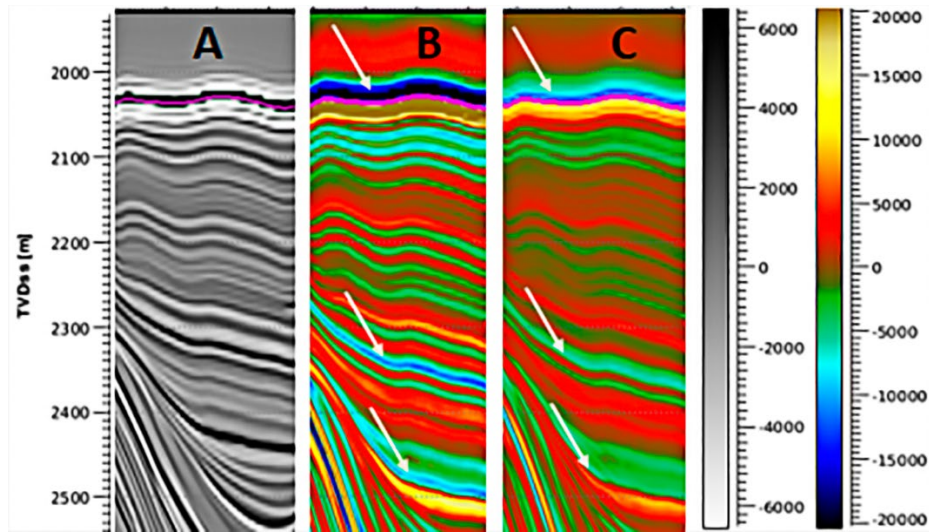


Figure 5 - A – Seismic amplitude in depth; B – Integrated seismic amplitude in rainbow pallet with some lateral lobes indicated by the white arrows; C – Band-pass acoustic impedance with white arrows showing the lateral lobe attenuation.

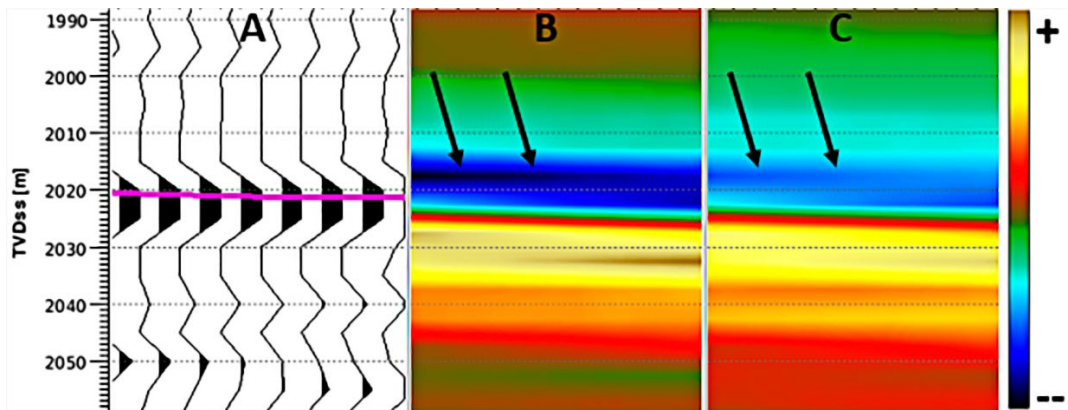


Figure 6 - Magnified view of Figure 5. A – Seismic amplitude in depth with seabed horizon; B – Integrated seismic amplitude in rainbow pallet with the lateral lobe indicated by the arrows; C – Band-pass acoustic impedance with the negative lateral lobe indicated by the arrows.

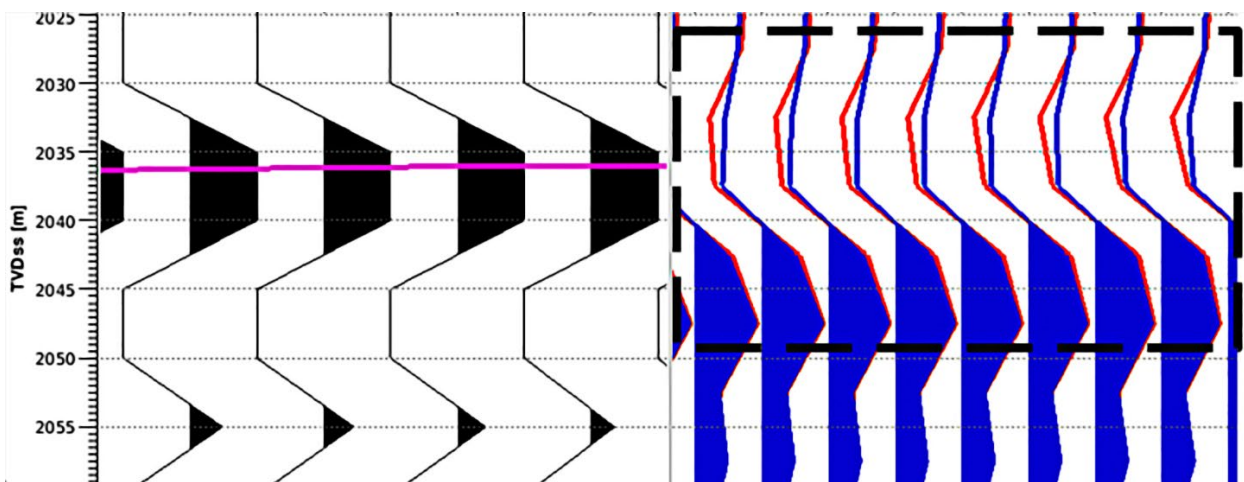


Figure 7 - Left panel - Seismic amplitude in depth with seabed horizon; Right panel - Integrated seismic amplitude in red and Band-pass acoustic impedance. The dashed rectangle illustrates the negative lateral lobe, much less expressive in blue than in the red data.

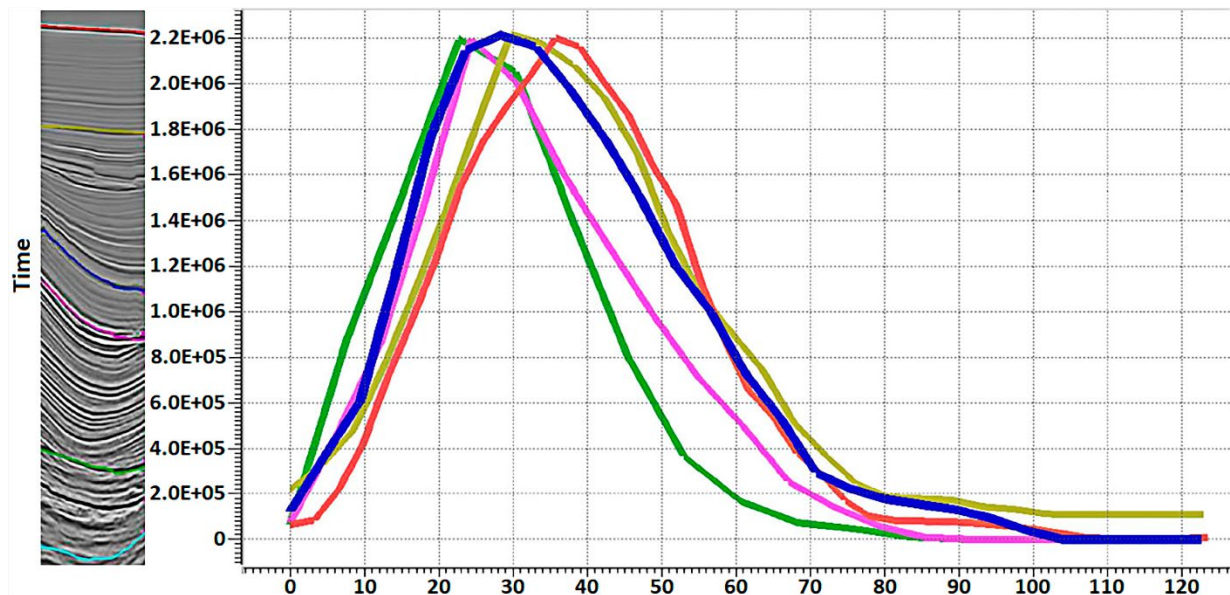


Figure 8 - Normalized wavelet frequency (Hz) spectrum throughout the burial depth effect. The wavelets were extracted from the amplitude seismic data. The red one reflects the layer between the top of Marambaia Formation and the top of Itajaí-Açu Formation. The yellow wavelet encapsulates in the layer between the top of Itajaí-Açu Formation and the top of Guarujá Formation. The blue wavelet was extracted from the layer between the top of Guarujá Formation and the top of Ariri Formation. The purple wavelet considers the layer between the top of Ariri Formation and the top of Barra Velha Formation. The green wavelet was extracted from the layer between the top of Barra Velha Formation and the base of Barra Velha Formation.

It is also essential to review the described rock types during the well drilling. Figure 9 shows the interpretation changings in the rock type logs. The color palette for the well log rock type is light green for claystone, dark green for shale, yellow gold for sandstones, light blue for silty shale and blue for marl. The left track presents the interpretation according to the mud log description, and the right one presents the reviewed rock types based on other acquired logs (spectral gamma ray, resistivity) as supplementary information.

In portions with absence of well logs (P/S-sonic and density), it was used the amplitude vs. offset (AVO) analysis within the seismic bandwidth to estimate the geohazards. For each interval restricted by a top and base picked seismic horizon layer, it was calculated the layer seismic attributes Band-Pass P-Impedance (IP_BP) and Integrated gradient (Grad), using Aki-Richards' two-term AVO equation (Rosa, 2018). Figure 10 shows the post-salt section of the IP_BP attribute, the available nine seismic horizons in black and the rock descriptions described for each well.

In the salt section, in order to characterize the salt lithologies, it was performed a deterministic

acoustic and model-based constrained sparse spike inversion (CSSI). Because in general the salt section contains a minimum well log suite with P-Sonic and Density, it allows building the prior model that is a low frequency P-impedance model guided by the picked seismic horizons and wells.

Figure 11 illustrates the amplitude seismic section for the salt section of the studied areas, the well log P-impedance and the 3 picked horizons named as Top of Salt; Intra-Salt, which splits the stratified portion from the homogenous Salt; and the Base of Salt.

Figure 12 presents the full band inverted P-impedance for the salt section. Despite the leftmost well not being used in the prior model, there was a good match between the inverted P-impedance and the well log P-impedance.

To deal with the uncertainty analysis, which involves the static elastic property estimation in the main production pre-salt reservoir, the Barra Velha Formation (Carminatti et al., 2008), we conducted static vs. dynamic hydrostatic compression tests. We used the Pontifical Catholic University's Rock Test Lab using roman travertine core samples as mechanical analogues of the good quality carbonate

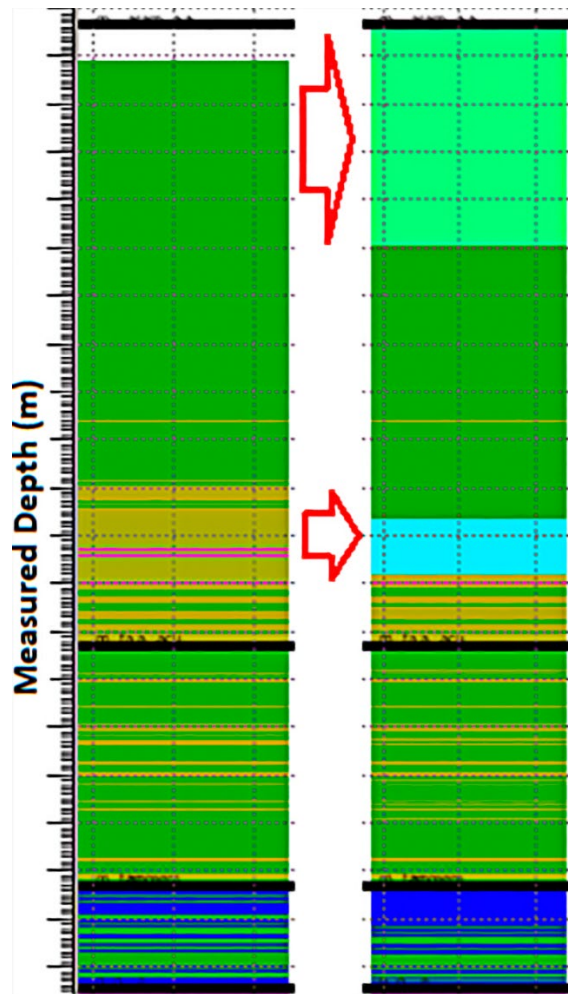


Figure 9 - Changings in the rock type log. The left track is the interpretation considering purely the of the cutting sample description collected from the mud and the right one is the interpretation taking auxiliary logs (spectral gamma ray and resistivity).

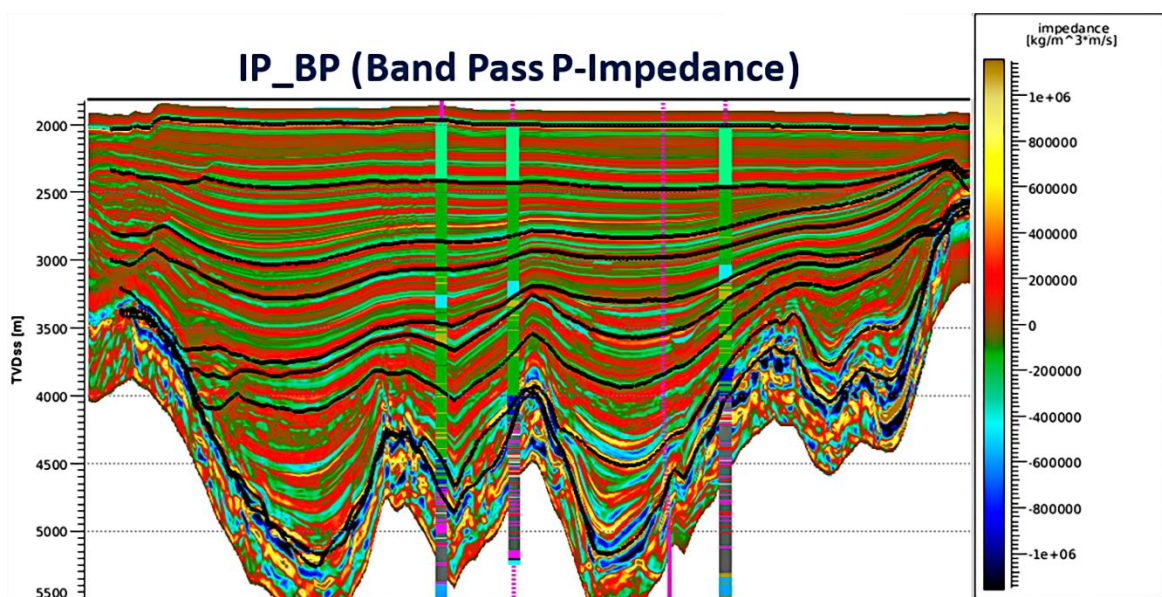


Figure 10 - Band-pass P-impedance in depth for the post-salt layer, picked seismic horizons and rock description for the wells.

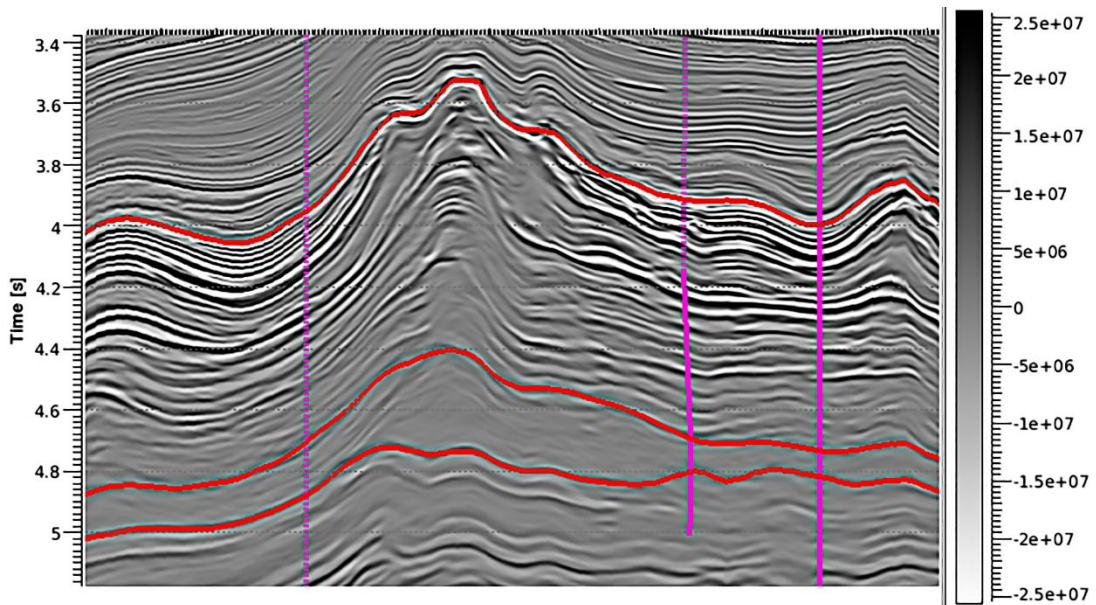


Figure 11 - Seismic amplitude in time, illustrating the salt section, the 3 horizons used for the inversion process (Top of Salt, Intra-Salt and Base of Salt) and the well tracks in purple.

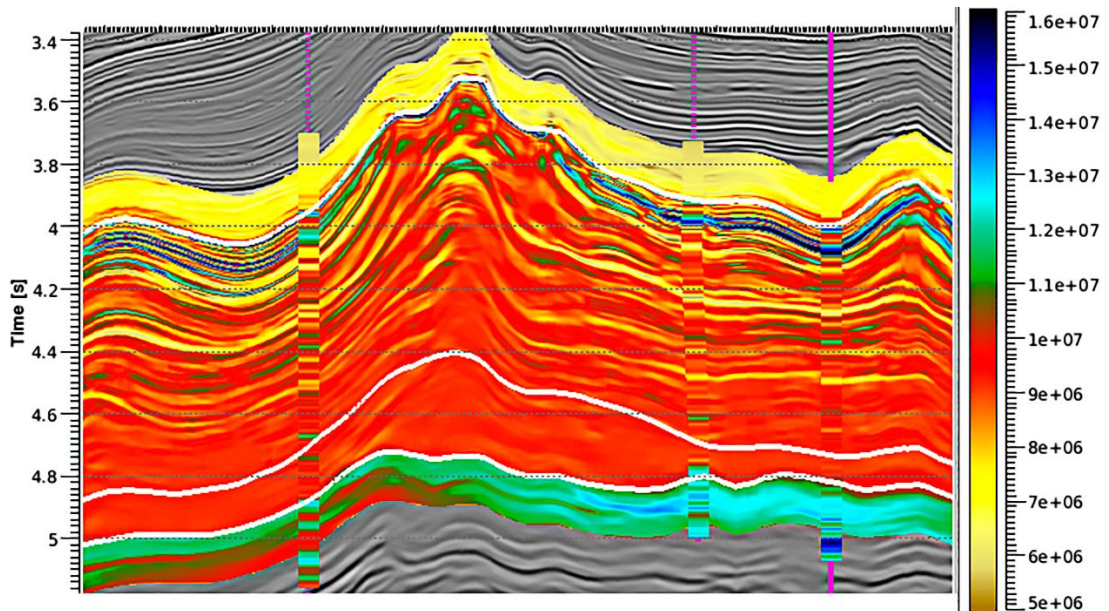


Figure 12 - Full band inverted P-impedance for the salt section in time. It can be seen a great matching between well logs and the P-Impedance attribute delivered for the inversion process, even for the leftmost well not included in the prior model.

reservoirs, since both have the same mineral composition: calcite and the high porosity roman travertine with some dissolutions. There were five samples with 108mm height, 54mm diameter and 10% to 13% porosity. To reach as close as possible the confining stresses in the reservoir since the samples presented high porosity, a hydrostatic test was carried out to avoid the emergence of deviatoric stresses and so break the sample too early. In this laboratorial test, an ultrasonic P and S wave

pulse from piezoelectric crystals up to the frequency of 250 KHz, representing the dynamic branch, is passed through the dry samples while it is hydrostatically compressed by the fluid (water) and also vertically compressed by a steel press inside a hydraulic vessel. The available seismic data have the main dominant frequency peak around 25 Hz in the carbonate reservoirs. Nevertheless, the ultrasonic waves were taken as a valid dynamic branch, since the calcite sample cores were dried before the rock testing

labs and the porous system was well connected.

Figure 13 illustrates the roman travertine block and the arrangement for the simultaneous hydrostatic compression test, performed at PUC's Rock Test Lab (Meneguim, 2019).

In Figure 14 it is shown an ultrasonic P-wave (blue) traveling through the travertine sample while the static compression by the steel press is carried out in the 0.5 MPa/min compression rate. It is also shown the first break mark picked (red) corresponding to the P-wave arrival time, according to the proceedings found in Morschbacher et al. (2010) and applied in Meneguim (2019). The P-wave and S-wave in Figure 15 were filtered by a 70-160 KHz band-pass filter to eliminate spurious noise and allow the correct first break estimation. The S-wave arrival times were picked from the first break mark that corresponds to a negative peak in the ultrasonic S-wave as illustrated in Figure 15.

The S-wave arrival times were picked from the first break mark that corresponds to a negative peak in the ultrasonic S-wave as illustrated in Figure 15.

The system times, the necessary times for the P and S ultrasonic waves pass through the whole electric circuit, without any core sample in the system were also recorded: 14.10 μ s for P-wave and 17.30 μ s for S-wave. The P and S-wave velocities are estimated from the difference between picked arrival time and system time considering the 108 mm sample height for each instant in the hydrostatic compression branch.

In Figure 16 it is exhibited the applied continuous loading during the testing time for the sample core T03.

For core sample T03 it was possible to reach the maximum confining stress of 22 MPa like the target confining stress in the reservoir around 20MPa. For the other 4 samples, the rubber membrane that isolates the sample from fluid (water) inside the hydraulic vessel broke too early for a confining stress around 15 MPa.

Once the rubber membrane is violated for a

confining stress larger than 22 MPa and a testing time longer than 2600 s, the sample core becomes wet by water and the pore pressure becomes accumulated inside the sample porous making the dataset unappropriated. For this reason, the dataset after the testing time 2600 s was discarded. T03 sample had a lower superficial porosity, so the deformations in the rubber membrane involving it were less expressive and this sample offered the best acquired dataset.

In Figure 17 it is shown the volumetric strain versus the confining stress for sample core T03.

The volumetric strain was calculated by summing the axial strain plus two times the radial strain of the LVDT displacement sensors attached to the sample. The static compressibility modulus for each testing time came from the tangent straight line in Figure 17.

Figure 18 exhibits the obtained dynamic vs. static volumetric compressibility modulus from the hydrostatic compression test.

The resulting dynamic vs. static equivalence for the volumetric compressibility modulus corresponding to the straight line in Figure 15 obtained from PUC's Rock Test Lab (Meneguim, 2019) is given by the following equation:

$$K_{Bsta} = 1.089 K_{Bdyn} - 22.313 \text{ (GPa)} \quad (1)$$

It is possible to demonstrate that the variation of the elasticity modulus for the carbonate reservoirs is almost ten times higher when considering the lower porosity carbonates compared with the higher porosity ones. On the other hand, the Poisson's ratio variation is smaller when considering the lower porosity carbonates compared with the higher porosity ones. These statements were done after the log analysis of more than one hundred pre-salt section drilled wells in the Santos Basin. From our observation, we can state that the elasticity modulus for porosity lower than 3% is around 60 GPa, and for porosity higher than 20% is about 8 GPa. For the Poisson's ratio, it is observed 0.29 for low porosity and 0.23 for high porosity, denoting a small variation. Therefore, as the elasticity modulus

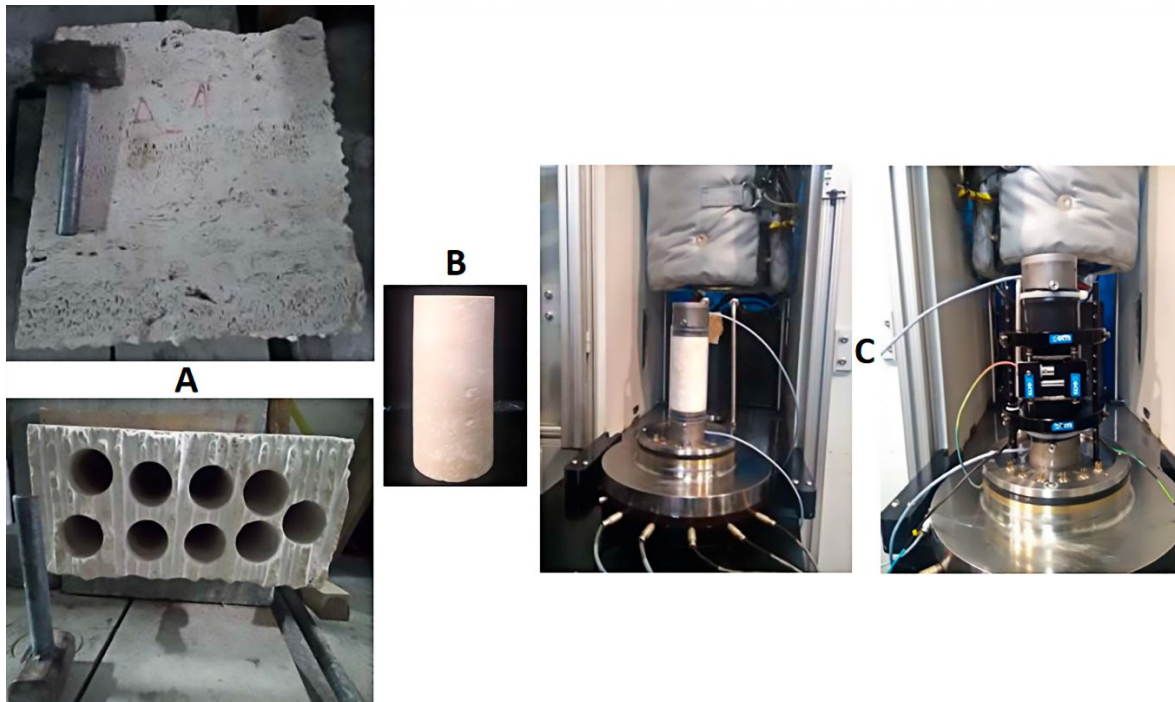


Figure 13 - A – The roman travertine block – the upper image shows the block view and the bottom one shows the rotated view with the plug holes; B – the plug used for the test; C – the test preparation, the positioning of the plug in the equipment on the left and details of the LVDT sensors attached to the sample to measure its axial and radial displacements.

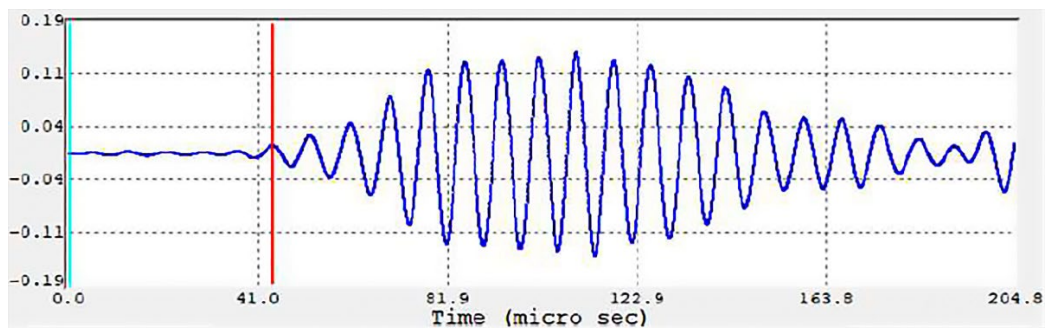


Figure 14 - Ultrasonic-P pulse traveling through the travertine sample at the time 240 s vs. the voltage of the hydrostatic compression test. Also, the compressive wave (blue) and the first break mark picked (red) corresponding to the P-wave arrival time (Meneguim, 2019).

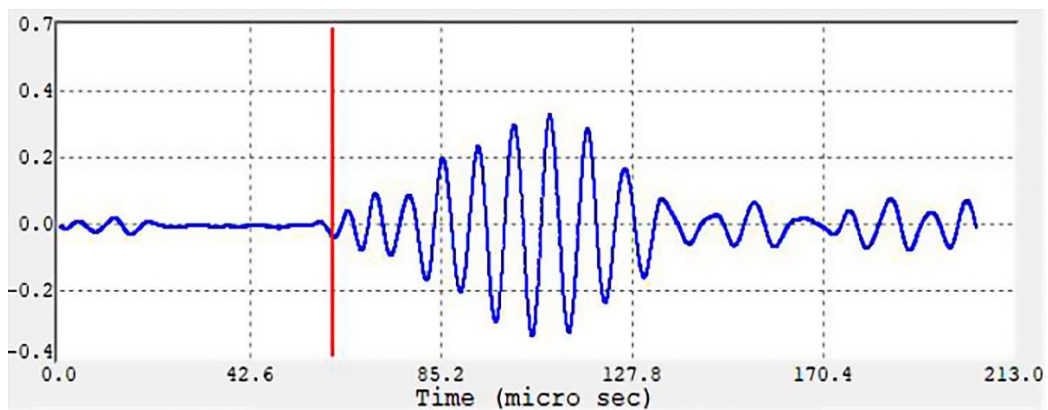


Figure 15 - Ultrasonic-S pulse traveling through the travertine sample at the time 240 s vs. the voltage of the hydrostatic compression test. Also, the shear wave (blue) and the first break mark picked (red) corresponding to the S-wave arrival time (Meneguim, 2019).

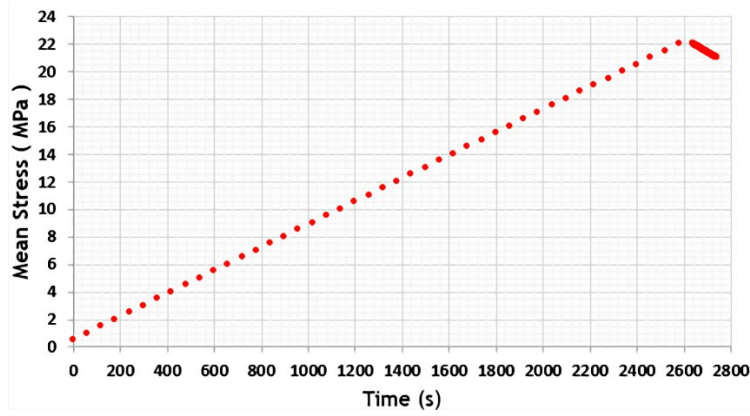


Figure 16 - The testing time (s) versus the confining stress (MPa) for the core sample T03.

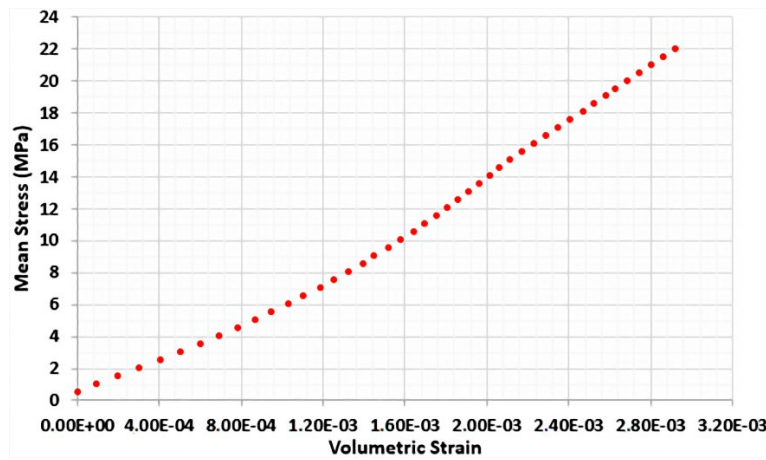


Figure 17 - The volumetric strain versus the confining stress (MPa) for core sample T03.

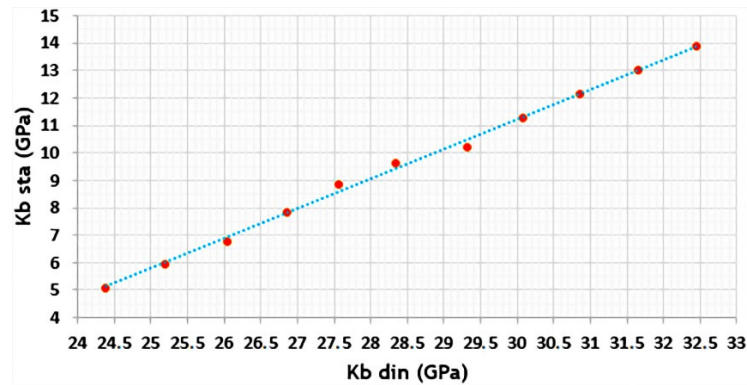


Figure 18 - Dynamic vs. static equivalence for the volumetric compressibility modulus obtained in PUC's Rock Test Lab for sample core T03.

variation in this media is the dominant parameter for Equation 1, the static-dynamic equivalence for dry rock for this parameter was calculated from the equation. As we assumed that the Poisson's ratio variation is secondary, for this parameter the static-dynamic equivalence for dry rock was considered as one to one.

In Table 1, we exhibit the three statics vs. dynamic equivalences of dry rock for the elasticity modulus, including the ones mentioned in the introduction section and the one presented in equation 1, used to access the uncertainties in the static elastic elasticity modulus estimates of the pre-salt portion. The 1st and 2nd equivalences are very

Table 1 - The three equivalences for dry rocks used as dynamics vs. static elasticity modulus equivalences in the pre-salt, Santos Basin.

1 st Equivalence	$E_{sta} = 0.77 E_{dyn} + 5854.12$ (Pa) (Pandula & Mockovčiaková, 2002)
2 nd Equivalence	$E_{sta} = 0.478 E_{dyn}^{1.029}$ (GPa) (Lacy, 1996)
3 rd Equivalence	$E_{sta} = 1.09 E_{dyn} - 22.31$ (GPa) PUC's Rock Test Lab (Meneguim, 2019)

well-known parameters coming from scientific papers (Lacy, 1996; Pandula & Mockovčiaková, 2002) and the 3rd one was obtained from mechanical tests carried out in PUC's Rock Test Lab.

In the post-salt section, it was obtained a 3D seismic class model focusing on the most relevant geotechnical hazards coupled with anomalies in some seismic attributes: IP_BP (P-Impedance Band-Pass) and Gradient (Integrated gradient). In the next Figures (19 up to 28) it is presented the seismic classes from the oldest formation to the youngest one, in this case from Itanhaém Formation (Albian age) to Marambaia Formation (Neogene period). The rock color palette is light green for claystone, dark green for shale, light blue for silty shale, blue for marl, red for sandstone in the seismic attribute and yellow gold for sandstone in the well log rock types.

In Figure 19, it is illustrated the 3D seismic class model in deeper Itanhaém Formation in which the shale was modeled taking the low impedance values and the background marl was modeled by the remain impedance values. It can be seen that the obtained seismic class model is quite like the rock types in the wells for the packages thicker than the seismic resolution which is around 30 m.

Figure 20 illustrates the 3D seismic class model for the Itajaí-Açu Formation layer 1. Sand packages are in the low impedance and gradient values and the background shale is in the remaining sector.

In Figure 21 it is illustrated the 3D seismic class model for the Itajaí-Açu Formation layer 2. Thicker sand packages are in the low impedance and gradient values. In this layer, we got an exceptional agreement between the seismic class model and the rock types in the wells, since the

drilled packages were bigger than the seismic resolution and the seismic signal to noise ratio is highly closer to 10 for this layer.

In Figure 22 it is illustrated the 3D seismic class model for the Itajaí-Açu Formation layer 3. The shale is in the low gradient and impedance values and the background silty shale is in the remaining high gradient sector. In this layer we got the worst agreement between the seismic class model and the rightmost well, probably due to less sensitivity in the seismic attributes to separate the rock types of shale and silty shale, which have a very similar attribute signature. We believe the seismic quality is good in the Itajaí-Açu Formation layer 3, despite the worst efficiency in the seismic class model, since this model is working very well in the below and above layers.

In Figure 23 for the Itajaí-Açu Formation layer 4, it is showed the integrated gradient and we can identify a strongly negative gradient reflector corresponding to a sand package in the rightmost well. In Figure 24 this strong negative anomaly is drawn with a white polygon. In Figure 25 it is illustrated the 3D seismic class model for the Itajaí-Açu Formation layer 4, the sand package obtained from the negative gradient anomaly that exhibits a good agreement with the sand package in the rightmost drilled well.

Finally, we focused our attention on the shallowest and youngest sections of the post-salt, the Marambaia Formation. Figure 26 illustrates the AVO behaviour for the Seabed below the Seabed+700m using the cross-plot IP_BP (x-axis) vs. Integrated gradient (y-axis). It is interesting to point out, in Figure 26, that in the close seabed it is observed a strongly positive background line due to the high valued gradient layers in the green arrows.

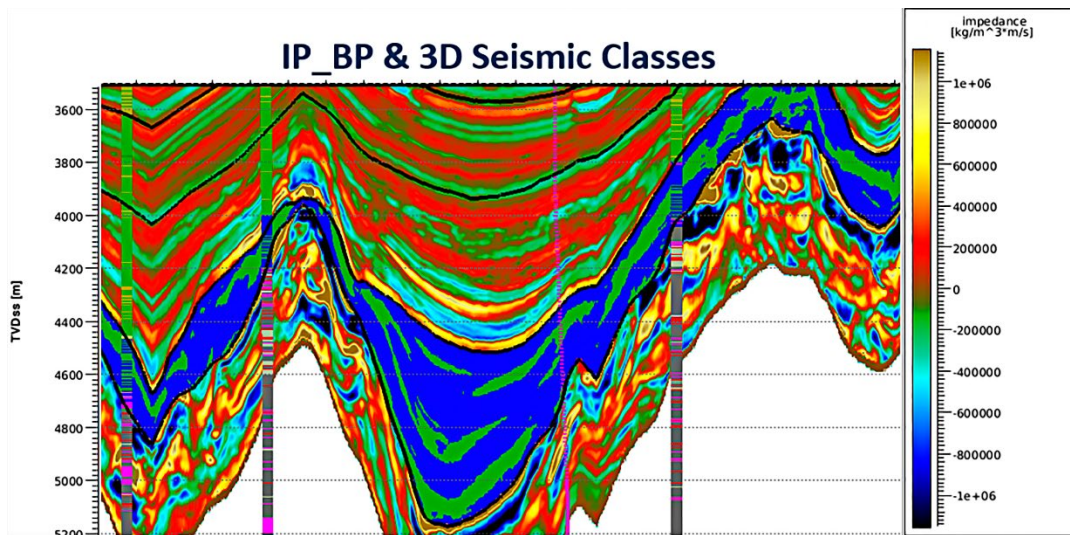


Figure 19 - 3D section of Itanhaém Formation presenting the seismic class attribute results.

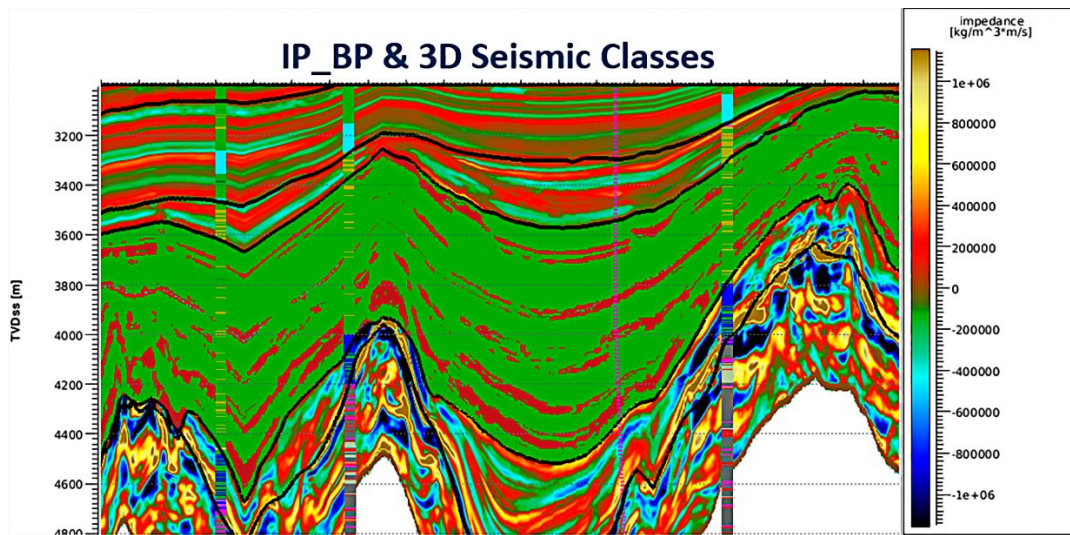


Figure 20 - 3D seismic classes in Itajaí-Açu Formation layer 1.

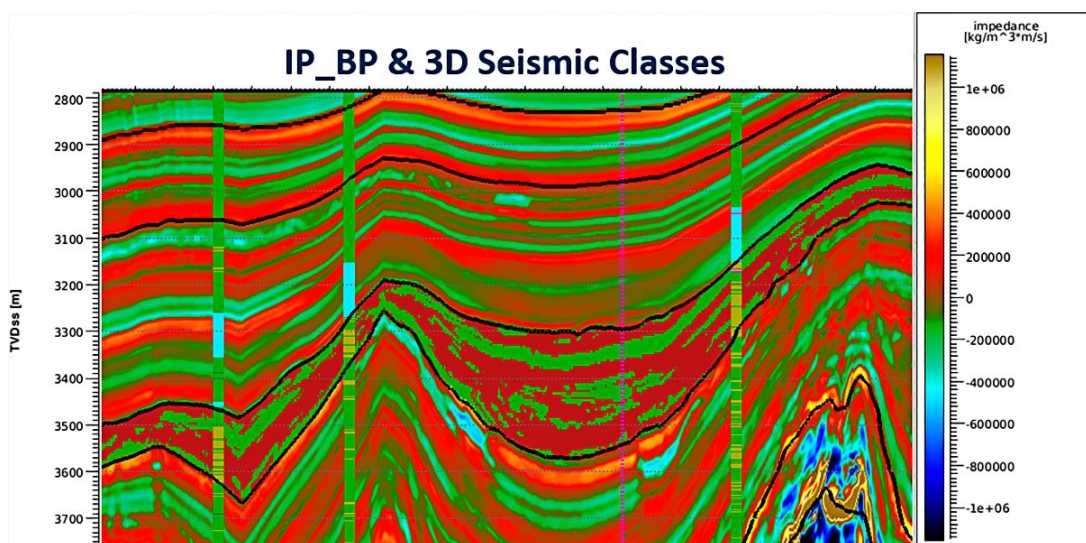


Figure 21 - 3D seismic classes in Itajaí-Açu Formation layer 2.

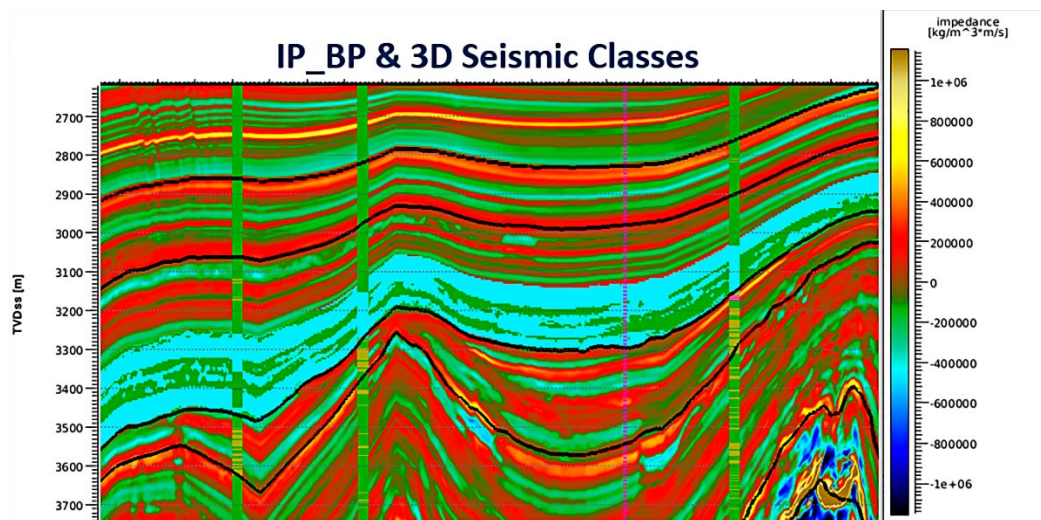


Figure 22 - 3D seismic classes in Itajaí-Açu Formation layer 3.

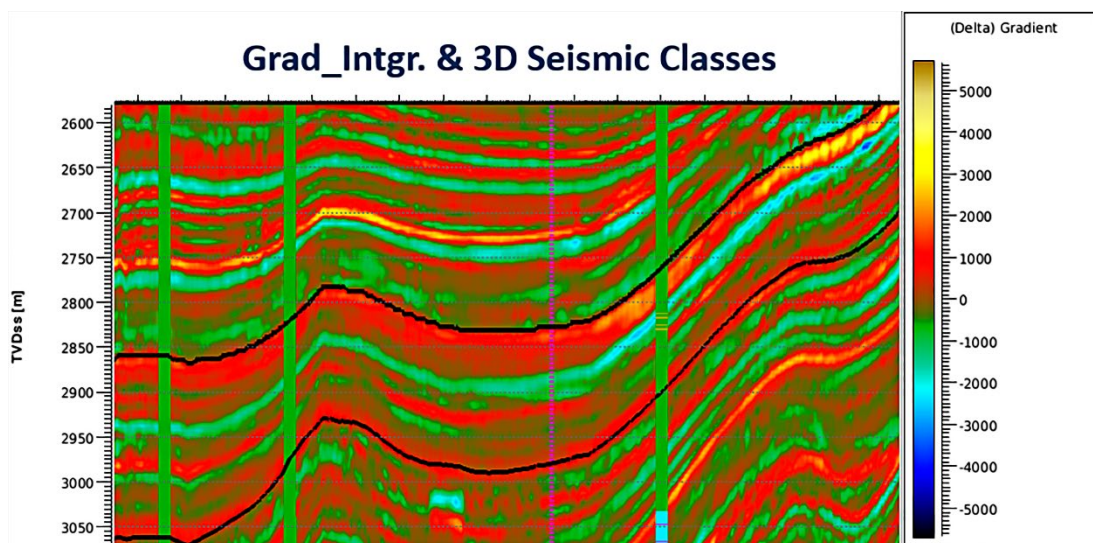


Figure 23 - 3D Integrated gradient in Itajaí-Açu Formation layer 4.

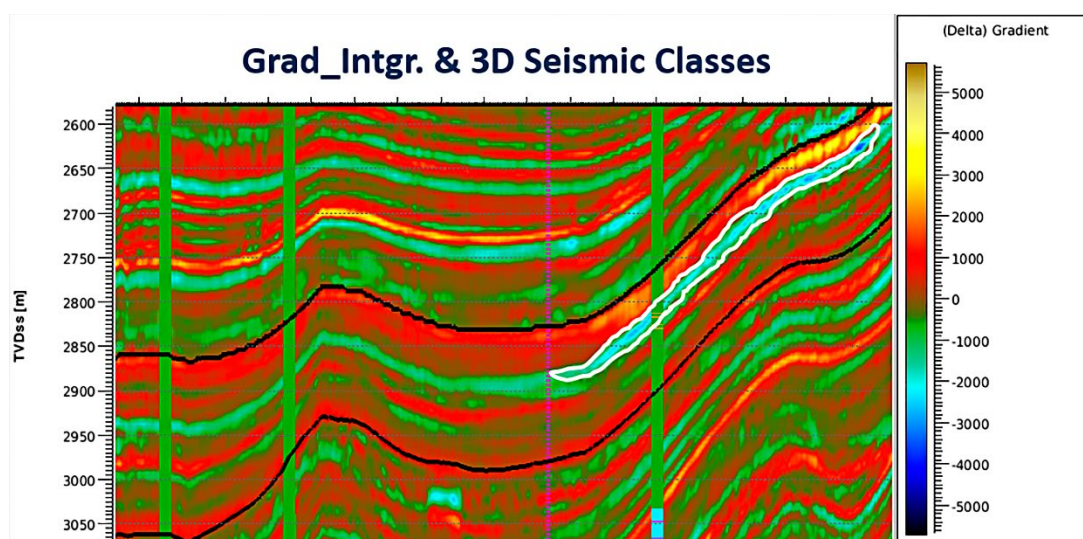


Figure 24 - 3D Integrated gradient attribute with the white polygon corresponding to a strong negative anomaly associated with the sand package in the drilled rightmost well.

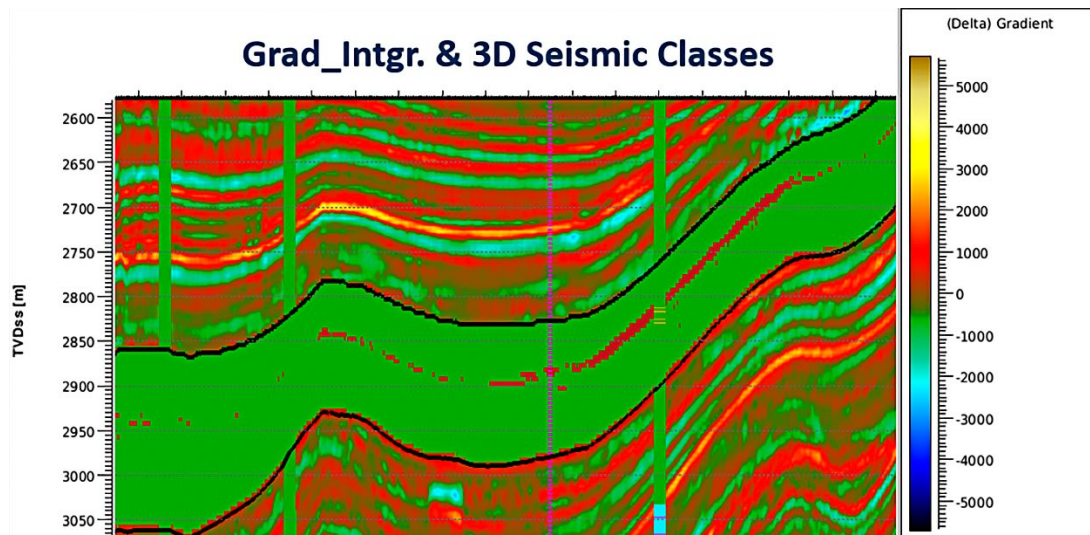


Figure 25 - 3D seismic classes in Itajaí-Açu Formation layer 4. The red class exhibits a good match to the sand package in the rightmost drilled well.

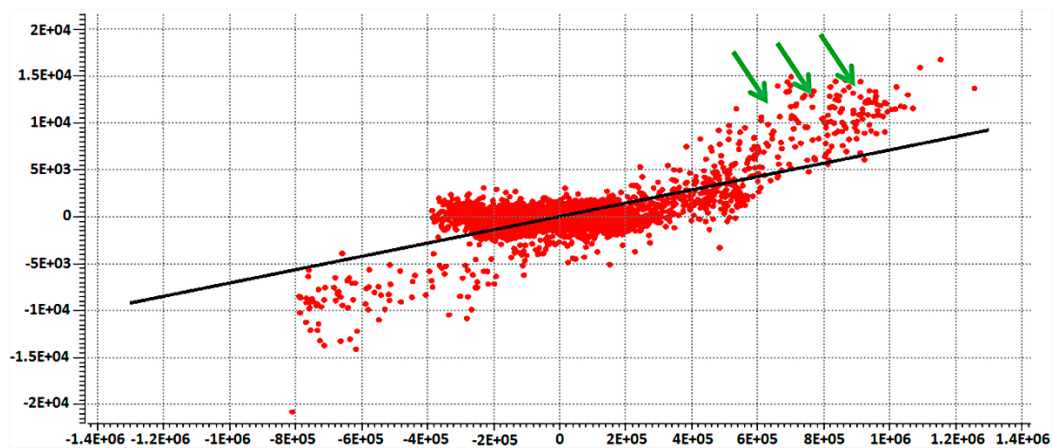


Figure 26 - For the seabed below the seabed+700m, the cross-plot IP_BP (x-axis) vs. the Integrated gradient (y-axis) shows the high valued gradient layers highlighted by the green arrows and a positive slope background straight line in black colour adjusted to the red points.

In fact, analyzing the amplitude in the black seabed positive peak reflector, it is observed that the FAR amplitude is bigger than the NEAR amplitude, probably due to highly hydrated unconsolidated sediments closer to the seabed as shown in Figure 27.

Analysing the study area, near to the three drilled wells, the seabed presents highly hydrated claystone rock type occurrences. Since these wells in the first phase are drilled without fluid return, we are blind to rock types of the intercalations of the sand packages and shale detection from the cutting samples, imposing a huge risk for this operation. Up to now, we have not detected any occurrences of geohazards in this portion for the study area. We defend that the joined work team decision, adopting the 3D seismic class model filled with claystone

rock type close to the seabed (Marambaia Formation), was one of the major responsible for the operational success. Figure 28 illustrates completely the 3D seismic classes in the post-salt section the focusing on the first 3 short-term geohazards listed in the beginning of this section.

In the salt section (Ariri Formation) we used another approach, adopting in this case probability density functions (PDF) from the drilled wells. Figure 29 illustrates the PDF from the borehole P-impedance and cutting sample logs following previous published strategies (Meneguim et al., 2015; Yamamoto et al., 2016). The relation between the salt lithotypes/minerals and P-impedance observed in Figure 26 supports the salt forecast based on the inverted P-impedance from the seismic data.

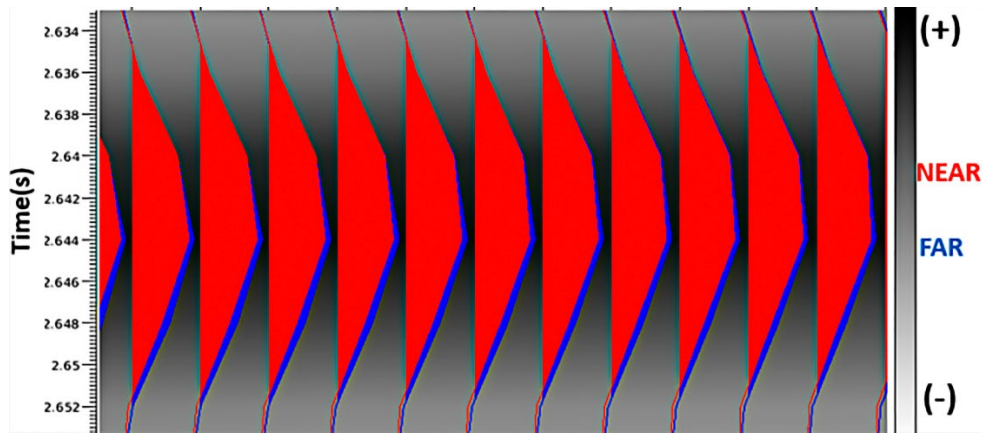


Figure 27 - In the black seabed peak reflector, the FAR amplitude is bigger than the NEAR amplitude, indicating the presence of highly hydrated and unconsolidated sediments.

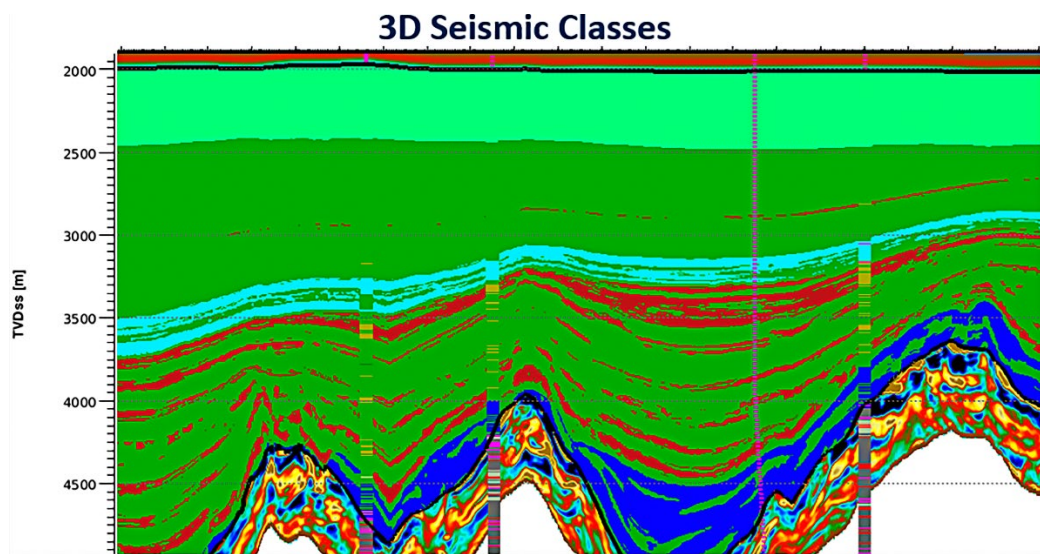


Figure 28 - 3D seismic classes in the post-salt section focusing on the main geohazards of this section. The rock color palette is light green for claystone, dark green for shale, light blue for silty shale, blue for marl, and red for sandstone in the seismic attribute and yellow gold for sandstone in well log rock types. The distance between the two leftmost wells is 3km.

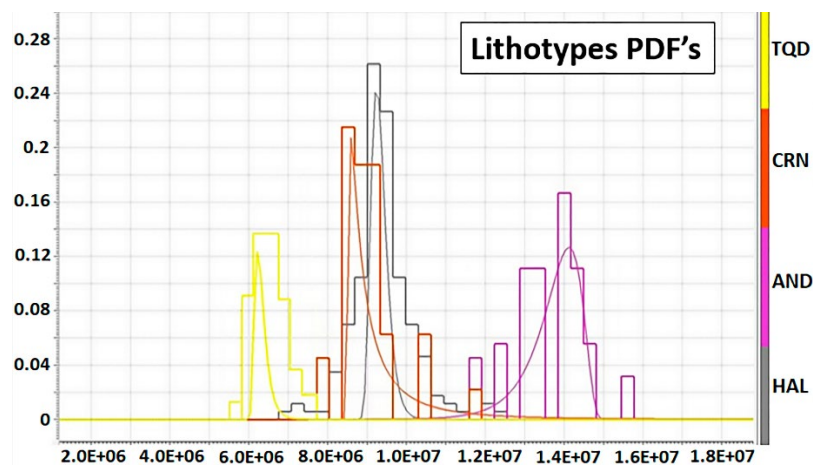


Figure 29 - P-impedance ($\text{kg/m}^3 \cdot \text{m/s}$) well log histogram for each salt rock/mineral (in gray: HAL - halite, in purple: AND - anhydrite, in red: CRN - carnallite and in yellow: TQD - tachyhydrite). The Gaussian Probability Density Functions for each salt mineral are the Gaussian's curves.

In Figure 29 the worst salt in terms of mechanical behavior, which is responsible for many warnings (Maul et al., 2018; Maul, 2020) in drilling well operations, is the yellow one (tachyhydrite) located in the lowest P-impedance values. This mineral has lots of water in its composition ($\text{CaMg}_2\text{Cl}_6 \cdot 12\text{H}_2\text{O}$) and exhibits a highly creep behavior. Meneguim et al. (2015) illustrate in the salt section the probability volumes of each salt making use of the PDF for the salt's classification from seismically inverted P-impedance. They obtained a 3D seismic class model from the salt most likely to deliver a forecast of the salt section for a project in the Santos Basin Pre-Salt Province.

To investigate the salt forecast accuracy, a blind test was performed. Two wells were removed from the prior model used in the seismic inversion. In Figure 30, despite the rightmost and leftmost wells not being used in the prior model, the inverted full band P-impedance presented a satisfactory agreement to their P-impedance well logs.

In Figure 31, despite the rightmost and leftmost wells not being used in the seismic inversion, the most likely salt from the probability density function (PDF) classification over the inverted full band P-impedance presented a satisfactory agreement to their salt rock type well logs.

The salt section above the Santos Basin pre-salt reservoirs plays a central role in the E&P activities (Costa & Poiate Jr., 2009). As per these authors the salt acts as: a seal, since it has negligible porosity and permeability to reservoir fluids; thermal insulator due to its small thermal conductivity that allowed the hydrocarbon cook generation; and as deviatoric stress reliever, since it has small susceptibility to fault/fracture propagation due to its ductile component rather than the purely brittle behavior. To mention few salts found in the salt section besides the most frequent halite, we can cite soluble salts as carnallite and the more dangerous tachyhydrite, a highly soluble salt that is responsible for many pipe sticking occurrences during well perforation, since it creeps into the borehole direction. Also, there is the anhydrite, an insoluble salt presenting a more brittle behavior than the other salts, that can be responsible for undesired failure during well operations.

Due to the importance of the salt section, our seismic class model supports the salt heterogeneity characterization to detect the soluble salt (tachyhydrite) with a highly creep behavior and anhydrites, since they generally cause the most relevant geotechnical hazards there.

In the pre-salt reservoir section, taking the 3D seismically inverted P and S-impedances, we directly computed the dynamic elastic deformability properties for the saturated rock frame using the elasticity theory (Rosa, 2018).

Figures 32, 33 and 34 exhibit the elasticity modulus (E), the Poisson's ratio and the Biot-Willis' coefficient, respectively, in another analyzed well location. In each Figure, the 4 curves represent the equivalent dynamic modulus obtained from seismics (in black); the static modulus obtained from the 1st equivalence (Pandula & Mockovčiaková 2002 - in blue); from the 2nd equivalence (Lacy 1996 - in green); and from the 3rd equivalence (Meneguim, 2019 - in red). The differences between these curves give us an idea of the uncertainty in estimating the mechanical behavior of the reservoir.

Since the three equivalences presented in Table 1 are for dry rocks, we used Gassmann's fluid substitution method (Smith et al., 2003) to consider the fluid effect on the elastic deformability properties for the saturated rock frame.

Analyzing the three mentioned equivalences for the dynamic-static equivalence, it was observed for the saturated rock frame in the reservoir that the static elasticity modulus varies up to 35% from the hardest equivalence (1st) to the softest one (3rd), the Poisson's ratio varies up to 22% and the Biot-Willis' coefficient varies up to 15%.

Scenario 1 (Pandula & Mockovčiaková, 2002) was the hardest scenario modelled and it is probably appropriate to cemented and low porosity rocks. Scenario 3 (Meneguim, 2019) equivalence was the softest one since the roman travertine samples had a high porosity and some dissolutions and it is probably appropriate to high porosity or even karst systems. Scenario 2 (Lacy, 1996) behaves as an intermediate scenario in terms of deformability properties.

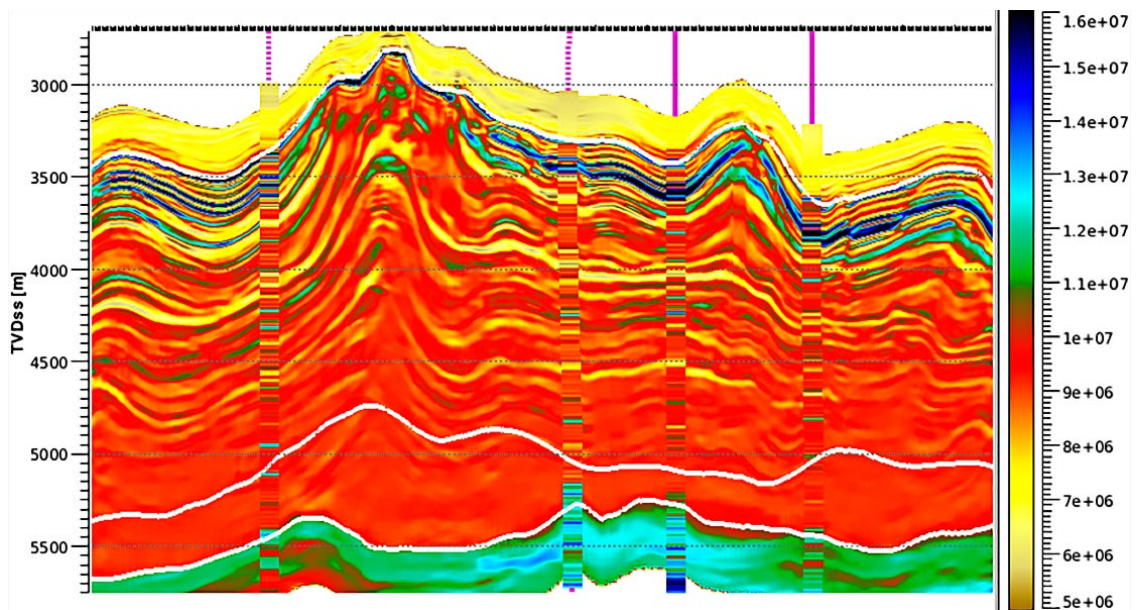


Figure 30 - Full band inverted P-impedance for the salt section in depth. It can be seen a great matching between well logs and the P-impedance attribute delivered by the inversion process, even for the leftmost and rightmost wells not included in the seismic inversion prior model. The three horizons used for the inversion process (Top of Salt, Intra-Salt and Base of Salt) are shown in white.

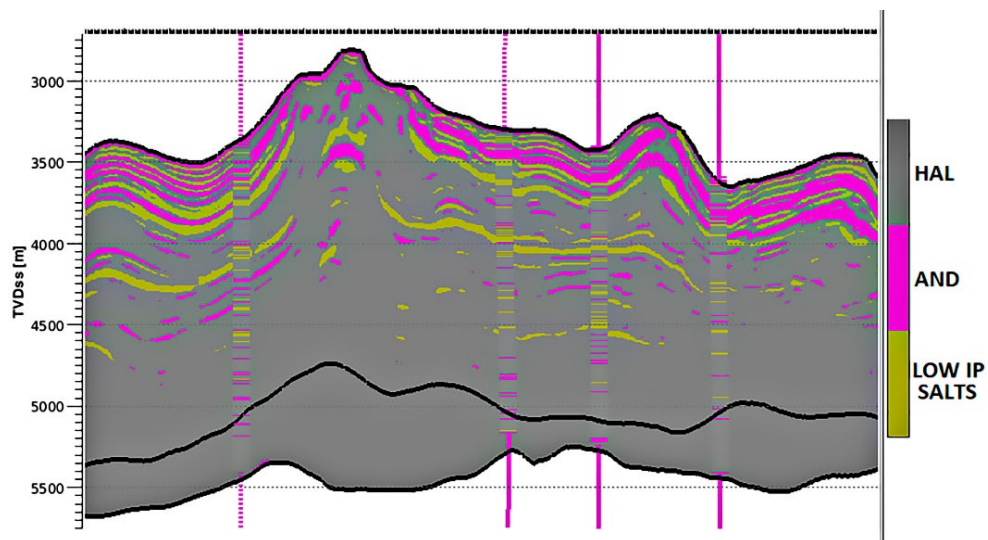


Figure 31 - Most likely salt from probabilistic density functions (PDF) over the seismically inverted full band P-impedance in depth. It can be seen a good matching between the salt rock type in the wells and the most likely salt delivered from the probabilistic classification, even for the leftmost and rightmost wells not included in the seismic inversion prior model. In yellow it is shown the low impedance salts: tathyhydrite and carnallite.

CONCLUSIONS

In this work, we show how seismic data can add to the building of complex geomechanical models for the pre-salt projects in Santos Basin, Brazilian offshore.

In the post-salt and salt sections, it was possible to model some important geotechnical hazards considering the burial depth effect on the

seismic data. Also, in the post-salt portion, we observe a connection between seismic attributes within seismic bandwidth, such as Band-pass P-impedance and Integrated gradient with the geotechnical hazards, and the short-term events. The events, such as kicks, drift diameter of the inside wall of a borehole, lost circulation in uncontrolled flow and pipe sticking in the salt

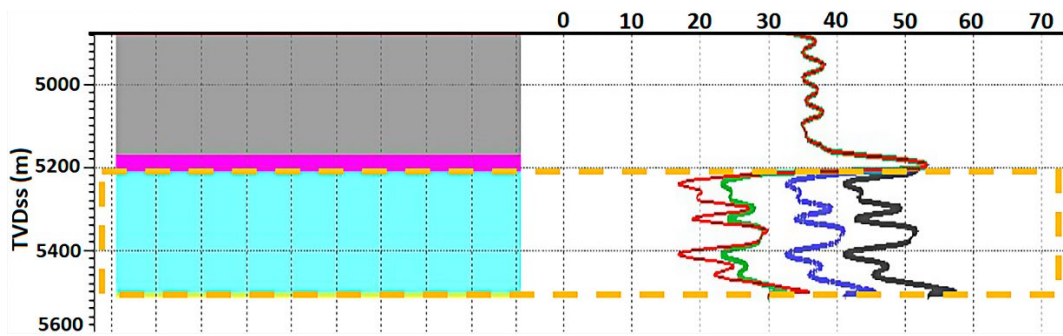


Figure 32 - Left panel - Carbonate reservoir in light cyan inside the yellow box, halite in gray and anhydrite in purple; Right panel - Elasticity modulus E (GPa) for the saturated rock frame in a given well location. Dynamic Elasticity modulus (black), 1st Static-Equivalence (blue), 2nd Static-Equivalence (green) and 3rd Static-Equivalence (red).

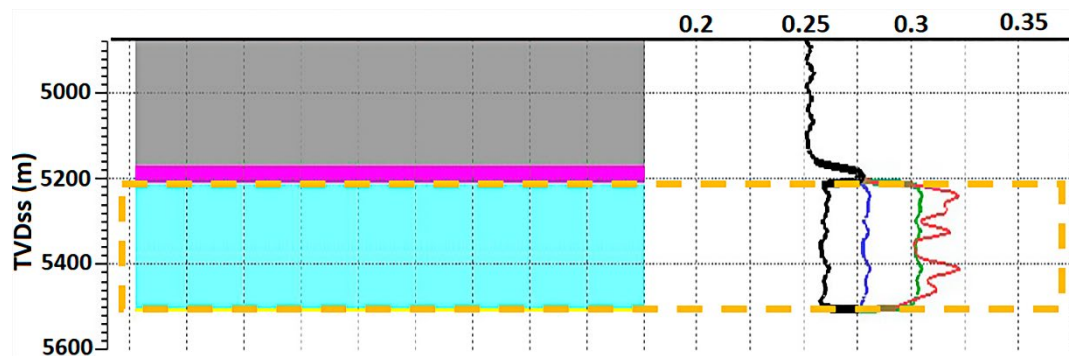


Figure 33 - Left panel - Carbonate reservoir in light cyan inside the yellow box, halite in gray and anhydrite in purple; Right panel - Poisson's ratio for the saturated rock frame in a given well location. Dynamic Poisson's ratio (black), 1st Static-Equivalence (blue), 2nd Static-Equivalence (green) and 3rd Static-Equivalence (red).

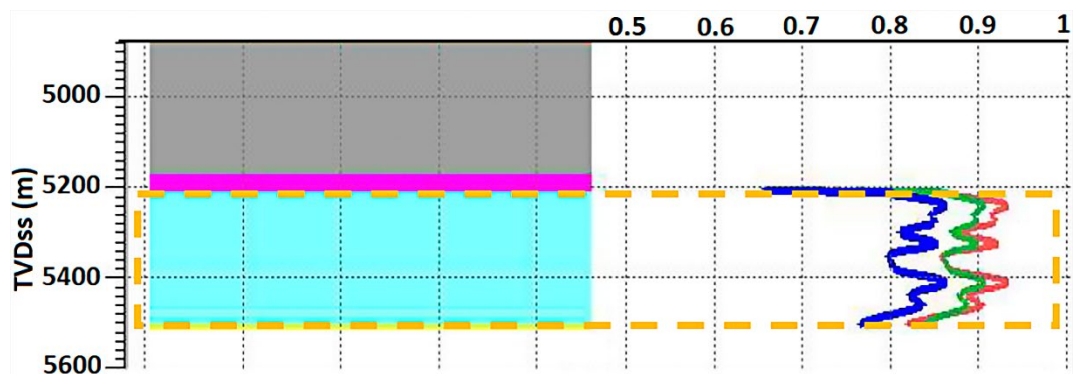


Figure 34 - Left panel - Carbonate reservoir in light cyan inside the yellow box, halite in gray and anhydrite in purple; Right panel - Biot-Willis' coefficient for the saturated rock frame in a given well location. 1st Static Equivalence (blue), 2nd Static Equivalence (green) and 3rd Static Equivalence (red).

portion, may occur during the drilling and completion well phases, and the seismically inverted full band P-impedance can help us identifying regions where these events might occur.

It is argued in this work that the first equivalence (Pandula & Mockovčiaková, 2002) was the hardest one and it is probably appropriate to cemented and low porosity rocks. The third

equivalence (Meneguim, 2019) was the softest one and it is probably appropriate to high porosity or even karst systems. The second equivalence (Lacy, 1996) behaves as an intermediate or base equivalence in terms of stiffness. These three static vs. dynamic equivalence relations involving modulus of elasticity enable us to explore the uncertainty issue in the pre-salt reservoir, in

Santos Basin. Comparing the three scenarios, we observe that the static elasticity modulus varies up to 35%, the static Poisson's ratio varies up to 22% and the Biot-Willis' coefficient varies up to 15%.

The authors are confident about the integration of the inverted seismic data into the geomechanical modeling workflow (Figure 3), using attributes to characterize geohazards in the Post-Salt and Salt sections, and to obtain the static elastic properties following the main workflow (Figure 4) exposed in this work. The implications will be safer operations during the lifespan of these complex Brazilian pre-salt reservoirs in Santos Basin.

ACKNOWLEDGMENTS

The authors would like to thank Petrobras for the permission to publish this work. Special thanks to Dr. Filipe Borges, for dedicating time to help to improve this manuscript with fruitful comments. We also thank the geologist Bruno Pinheiro Pires from PUC's post-graduation program as well as to the geophysicist Julio Justen from Petrobras for the support at PUC's Rock Test Lab.

REFERENCES

ANP – Agência Nacional do Petróleo, Gás Natural e Biocombustíveis. 2003. Reservas Nacionais de Petróleo e Gás Natural 31 Dec 2001. Superintendência de Desenvolvimento e Produção - SDP/ANP. Rio de Janeiro, RJ, Brazil. Available on: <https://www.gov.br/anp/pt-br/centrais-de-conteudo/dados-estatisticos/reservas-nacionais-de-petroleo-e-gas-natural>

ANP - Agência Nacional do Petróleo, Gás Natural e Biocombustíveis. 2015. Reservas Nacionais de Petróleo e Gás Natural 31 Dec 2014. Superintendência de Desenvolvimento e Produção - SDP/ANP. Rio de Janeiro, RJ, Brazil. Available on: <https://www.gov.br/anp/pt-br/centrais-de-conteudo/dados-estatisticos/reservas-nacionais-de-petroleo-e-gas-natural>

CARMINATTI, M., WOLFF, B. & GAMBOA, L. 2008. New exploratory frontiers in Brazil. Paper WPC-19-2802 presented at the 19th World Petroleum Congress 29 June–3 July 2008, Madrid, Spain.

COSTA, A.M. & POIATE JR, E. 2009. Rocha salina na indústria do petróleo: aspectos relacionados à reologia e à perfuração de rochas salinas. In: MOHRIAK, W, SZATMARI, P. & ANJOS, S.M.C. (Eds.). *Sal-Geologia e Tectônica-Exemplos nas Bacias Brasileiras*. São Paulo, SP, Brazil: Beca Edições Ltda., p. 362–385.

LACY, L.L. 1996. Dynamic Rock Mechanics Testing for Optimized Fracture Designs. In: 1997 SPE Ann. Tech. Conf. & Exhib. held in San Antonio, Texas, USA. 5-8 October. SPE paper 38716.

MAUL, A. 2020. Caracterização Sísmica da Seção Evaporítica Salina e suas Aplicações nos Projetos de Exploração, Desenvolvimento e Produção de Hidrocarbonetos. Doctor's Thesis. UFF. Niterói, RJ, Brazil. 250 pp.

MAUL, A., CETALE, M.A. & SILVA, C.G. 2018. Few Considerations, Warnings and Benefits for the E&P Industry when Incorporating Stratifications inside Salt Sections. *Brazilian Journal of Geophysics*, 36(4): 461–477. Doi: 10.22564/rbgf.v36i4.1981.

MENEGUIM, T.B., MENDES, S.C., MAUL, A.R., FERNANDES, L.F., FARIAS, M.G. & GONZÁLEZ G. 2015. Combining seismic facies analysis and well Information to guide new interval velocity models for a pre-salt study, Santos Basin, Brazil. In: 14th International Congress of the Brazilian Geophysical Society & Expogef, Rio de Janeiro, RJ, Brazil: SBGf. Doi: 10.1190/sbgf2015-271.

MENEGUIM, T.B., PEREIRA, C.E.L., ALMEIDA JR, M.P., BORN E., PROENÇA T., & GOMEZ L. 2017. Effects of Post Stack Seismic Data Conditioning on Impedance Inversion for Reservoir, Santos Basin, Brazilian Pre-Salt. In: 15th International Congress of the Brazilian Geophysical Society & Expogef, Rio de Janeiro, RJ, Brazil: SBGf.

MENEGUIM, T.B. 2019. Integração Sísmica-Geomecânica no Pré-Sal Brasileiro, Bacia de Santos. (Master's Thesis), 102–190 - Departamento de Engenharia Civil e Ambiental, Pontifícia Universidade Católica do Rio de Janeiro, RJ, Brazil: 200 pp.

MENEGUIM, T.B., VELLOSO, R., TARTARINI, A., YAMAMOTO, T., QUEIROZ, L. & ALMEIDA, M. 2019. Seismic Geomechanical Integration in the Brazilian Pre-Salt, Santos Basin. In: 16th International Congress of the Brazilian

- Geophysical Society & Expogef, Rio de Janeiro, RJ, Brazil: SBGf.
- MENEGUIM, T.B., ALMEIDA, T.P., GIACOMEL, R., SHIMIZU, V.K., TARTARINI, A., MAUL, A.R., & VELLOSO, R. 2021. Building Integrated Geomechanical and Seismic Data Models for the Brazilian Pre-Salt Reservoirs Development, Examples in the Santos Basin In: 17th International Congress of the Brazilian Geophysical Society & Expogef, Rio de Janeiro, RJ, Brazil: SBGf.
- MOHRIAK, W.U., SZATMARI, P. & ANJOS, S. 2012. Salt: geology and tectonics of selected Brazilian basins in their global context. In: ALSOP, G.I., ARCHER, S.G., HARTLEY, A.J., GRANT, N.T. & HODGKINSON, R. (Eds.). Salt tectonics, sediments and prospectivity. Geological Society, London, Special Publications, 363: 131–158. Doi: 10.1144/sp363.7.
- MOREIRA, J.L.P., MADEIRA, C.V., GIL, J.A. & MACHADO, M.A.P. 2007. Bacia de Santos. Boletim de Geociências da Petrobras, 15: 531–549.
- MORSCHBACHER, M.J., VASQUEZ, G.F. & JUSTEN, J.C.R. 2010. Metodologias de estimativa das velocidades sísmicas em ensaios de laboratório. In: 4o Simpósio Brasileiro da Sociedade Brasileira de Geofísica, DF, Brazil: SBGf.
- PANDULA, B. & MOCKOVČIAKOVÁ, A. 2002. Study of the Relation between the Static and Dynamic Moduli of Rocks, Metalurgija, 42(2002): 1,37–39.
- ROSA, A.L.R. 2018. Extracting Value from the Seismic Signal. In The seismic signal and its meaning. Chapter 4. Tulsa: SEG. p. 601–703. Doi: 10.1190/1.9781560803348
- SMITH, M.T., SONDERGELD, H.C. & RAI, S.R. 2003. Gassmann fluid substitution: A tutorial. Geophysics, 68: 430–440. Doi: 10.1190/1.1567211.
- TEIXEIRA, L., GOBATO, F., MAUL, A., CRUZ, N.M. GONÇALVES, C. & LAQUINI. 2017. Rock Physics and Seismic Inversion to identify stratification within salt section supporting velocity, facies modeling and geomechanical analysis. In: 15th International Congress of the Brazilian Geophysical Society, Rio de Janeiro, RJ, Brazil: SBGf, p. 5–10. Doi: 10.1190/sbgf2017-002.
- TORÍBIO, T., QUEIROZ, L.E., TEIXEIRA, L., YAMAMOTO, T., MENEGUIM, T., LEONARDO, L.M., CORTEZ, M., RELVAS, M.T., MOLITERNO, A.M., TARTARINI, A. & MAUL, A. 2017. Characterizing Evaporitic Section and Geomechanical Properties Using Seismic Inversion, a Case Study for Santos Basin. In: 15th International Congress of the Brazilian Geophysical Society. 2017. Rio de Janeiro, RJ, Brazil: SBGf. Doi: 10.1190/sbgf2017-226.
- YAMAMOTO, T., MAUL, A., BORN, E., GOBATO, F., CAMPOS, M.T. & GONZÁLES, M. 2016. Incorporação de Estratificações Salíferas na Modelagem de Velocidade de uma Jazida da Bacia de Santos. In: VII Simpósio Brasileiro de Geofísica, Ouro Preto – MG, Brazil: SBGf.
- ZOBACK, M. 2007. Wellbore stability. In: Reservoir Geomechanics: Part III - Applications. Cambridge: Cambridge University Press. p. 301–339. Doi: 10.1017/CBO9780511586477.011

T.B.M.: conceptualization (lead), formal analysis (lead), investigation (lead), methodology (lead), project administration (lead), software (lead), validation (lead), writing – original draft (lead); **T.L.P.A.:** conceptualization (supporting), investigation (equal), methodology (supporting), supervision (supporting), validation (supporting), writing – original draft (supporting); **R.S.G.:** conceptualization (supporting), investigation (equal), methodology (supporting), supervision (supporting), validation (supporting), writing – original draft (supporting); **V.K.S.:** conceptualization (supporting), investigation (equal), methodology (supporting), supervision (supporting), validation (supporting), writing – original draft (supporting); **A.M.N.T.:** conceptualization (supporting), investigation (equal), methodology (supporting), supervision (supporting), validation (supporting), writing – original draft (supporting); **A.R.M.:** conceptualization (supporting), investigation (supporting), methodology (supporting), validation (equal), writing – original draft (equal); **R.Q.V.:** conceptualization (equal), investigation (equal), methodology (supporting), validation (supporting), writing – original draft (supporting).

Received on December 29, 2021 / Accepted on May 26, 2022